# Polarimetric analysis of oil contaminated laboratory grown saltwater ice imaged by a ground based SAR

Marianne Myrnes, UiT The Arctic University of Norway, marianne.myrnes@uit.no, Norway
Camilla Brekke, UiT The Arctic University of Norway, camilla.brekke@uit.no, Norway
Laurent Ferro-Famil, Rennes 1, laurent.Ferro-Famil@univ-rennes1.fr, France
Chris Petrich, Northern Research Institute (Norut) Narvik, christian.petrich@norut.no, Norway

## Abstract

In this paper we present preliminary experimental results from a ground based SAR system imaging artificially grown saltwater ice induced with crude oil. The data is acquired from a large scale laboratory experiment conducted at the Arctic Environmental Test basin (AETB) at Hamburgische Schiffbau-Versuchsanstalt GmbH (HSVA) March 14 - April 4, 2017. Here two artificial ice types were generated with simulated seasonal variation consisting of an initial ice growth phase and a melting phase. Interpreting the uncalibrated full polarimetric intensity data acquired from the experiment show a potential for a more detailed polarimetric analysis for characterising the oil contaminated ice surface.

## 1 Introduction

The observed and predicted lows of Arctic sea ice extent have yielded increasing interest in the potential for new trans-arctic shipping routes as well as oil and gas exploration and development in the Arctic [1]. Oil spills near sea ice may lead to a complex range of oil in sea ice configurations. These type of configurations are dependent on the season and type of release [2][3].

Both space-borne and airborne synthetic aperture radar (SAR) systems play an important role in monitoring and characterising sea ice due to wide area coverage and its ability to operate regardless of weather conditions and sunlight. The literature comprises few studies on discriminating between sea ice and oil with SAR. A theoretical study was done by Brekke et al. [4] where their results show that there is potential for multi-polarization SAR systems to detect and discriminate between oil and newly formed sea ice. It is especially interesting to study thin sea ice ($< 0.3$ m ) since the backscatter signature of thin sea ice and oil are similar, making thin ice an oil lookalike. Brekke et al. [4] points out that there is lack of knowledge of the dielectric properties of freshly formed ice types and of oil properties in icy conditions.

Environmental risk and regulations make it a challenge to study interaction of oil in sea ice in the field. In order to simulate a likely oil in sea ice scenario, a large scale laboratory experiment took place at the Arctic Environmental Test basin (AETB) at Hamburgische Schiffbau-Versuchsanstalt GmbH (HSVA) March 14 - April 4, 2017. Here two artificial sea ice types, columnar and granular [5] were studied undergoing seasonal variation and interacting with crude oil.

A polarimetric Ground Based (GB) Synthetic Aperture Radar system, named (GB-PoSAR) developed by the SAPHIR team from Institut d'électronique et de télécommunications de Rennes (IETR) at the University of Rennes I, was used in the experiment. GB-PoSAR acquired multi-baseline acquisitions of the two ice types during the experiment. The measurements were done in X and C band, in co-, cross- and full polarization. The GB-PoSAR is a very high resolution system system with an incidence angle range of approximately 20 to 60 degrees. This gives us an unique opportunity to closely study the local electromagnetic properties of oil in saltwater ice. In this paper we present preliminary experimental results acquired from the GB-PoSAR system and we aim at characterising the oil contaminated artificial sea ice by polarimetry analysis and inversion of surface parameters.

## 2 Oil-in-ice experiment

The oil-in-ice experiment was a joint effort of two research projects under The Research Council of Norway (RCN); PETROMAKS2 *Microscale Interaction of Oil with Sea Ice for Detection and Environmental Risk Management in Sustainable Operations* (MOSIDEO), and *Centre for Integrated Remote Sensing and Forecasting for Arctic Operations*(CIRFA).

Two ice types were simulated. Type one: columnar ice was generated from freezing of still water that resulted in a one layer structure of the ice. Type two: granular ice was generated by disturbing the upper water column by fans blowing air slightly above the surface. This created a two layer structure of the ice and simulated sea ice formation in open leads.

Seasonal changes of sea ice were simulated by splitting

the experiment into five different phases. First an initial ice growth phase. Here the air temperature was lowered to -15 degrees celsius and the ice was allowed to grow to a thickness of approximately 0.2 m. Secondly, an insulation phase took place were a snow cover was simulated. This was done by insulating specific surface areas with styrofoam. This created a cavity beneath the insulated ice. Thirdly an oil injection phase, where a total of 280 $L$ crude (Troll B) oil was introduced underneath the ice. The oil gathered in the cavities beneath the ice. Then an encapsulation phase followed where the oil lenses were encapsulated within the ice. At the last phase, simulating spring melting season, the temperature was raised to -6 degrees celsius. Here the oil migrated up the brine channels and eventually ended up on top of the ice.

## 2.1 Experimental setup

**Figure 1** shows the test site at the AETB at HSVA. Here we see the two artificial sea ice types separated by a wooden barrier across the tank. The two ice types were further divided into different patches designated for remote sensing and microstructure ice sampling respectively. For each patch designated for oil interaction, an equivalent clean ice patch was present for comparison. On the columnar side an additional wooden barrier separates the reference clean ice side to the left and the oil contaminated ice to the right, see **Figure 1**. Throughout the experiment, both salinity measurements and core samples were taken. Temperature at the surface and in various depths of the ice column was logged continuously. The surface was monitored by several remote sensing sensors, herein a fluorescent sensor, an thermal IR camera, a ground penetrating radar and the GB-PoSAR. This paper only consider the data from GB-PoSAR.

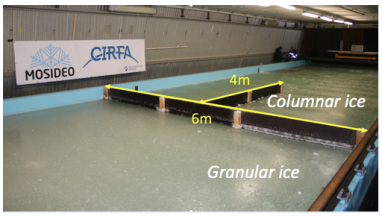


**Figure 1:** AETB experimental set up.

## 2.2 Data acquisition and processing

The set up of the GB-PoSAR can be seen in **Figure 2**. The system has been used in previous experiments concerning tomographic imaging of snow [6], and fjord ice [7]. The system consists of four horn antennas installed on a metallic box mounted on a linear rail. This was all fixed on a lift table. Inside the metallic box, a Vector Network Analyzer (VNA) controls the transmission and reception of the radar signals. A stepped motor is used to displace the system along the rail, producing an effective aperture length of maximum 3 $m$. The four horn antennas are displaced in azimuth and elevation producing six equivalent tracks when moved along the rail. By adjusting the height of the lift table, additional tracks are made. The SAR data are focused using the time domain back projection algorithm (TDBP). The GB-PoSAR system parameters can be found in **Table 1**.


**Figure 2:** GB-PoSAR set up. Upper left corner shows the alignment of the four horn antennas.

| GB-PoSAR | system parameters |
|---|---|
| Frequency band | X and C |
| Center frequency | 10.4 GHz and 5.8 GHz |
| Bandwidth | 4 GHz |
| Dynamic range | $\approx$ 90 dB |
| Polarization | VV, VH and HH |
| Azimuth aperture | 3 m and 1.5 m |
| Incidence angle $\theta$ | $25° - 60°$ |
| Resolution azimuth | 0.03 m |
| Resolution range | 0.0375 m |

**Table 1:** GB-PoSAR system parameters.

# 3 Polarimetry analysis and inversion of surface parameters

When characterising the surface scattering, we must consider the surface geometry and the dielectric properties. The complex permittivity of a medium is described as:

$$\epsilon = \epsilon^{'} + j\epsilon^{''} \tag{1}$$

Here $\epsilon^{'}$ represents the permittivity of the medium and gives the contrast with respect to free space while $\epsilon^{''}$ is the dielectric loss factor of the material. The geometrical characteristics may be described by the roughness height measurement, denoted as the standard deviation $s$ and the surface correlation length $l$, which can be interpreted as how fast the surface height changes. Assuming that the saltwater ice is relatively smooth, the surface scattering is modelled by the well known Small Perturbation Method (SPM) [8] [9]. The SPM assumes that $s$ and $l$ is small compared to the radar wavelength $\lambda$ [10], thus we

can express the vertical and horizontal surface variation as $ks$ and $kl$ where $k$ is the wave number: $2\pi/\lambda$.
The validity range of the SPM has been studied theoretically and by experiments, and is approximated to as $ks < 0.3$ and $kl < 3$ [10]. Under the SPM scattering model, and when considering the special case of backscattering, the first-order scattering coefficient is expressed as [10]:

$$\sigma_{qp} = 8k^4\sigma_1^2 \cos^4\theta_i |a_{qp}| W(2k\sin\theta_i, 0) \quad (2)$$

Here the subscripted *qp* denotes either incident field polarization $p$, or scattered field polarization q. $\theta_i$ is the local incidence angle, W is the Fourier transform of the surface correlation coefficient, and the polarisation amplitudes are represented by $a_{hh}$ and $a_{vv}$, $(a_{vh} = a_{hv} = 0)$. These are functions of the complex permittivity $\epsilon$ and $\theta_i$ only. The ratio of $a_{hh}$ and $a_{vv}$ (copolarization ratio) can be utilised to form a nonlinear equation and for a given $\theta_i$ be resolved for the permittivity $\epsilon^{'}$. When considering a Gaussian correlation coefficient, W corresponds to an isotropic roughness spectrum, and is a function of $kl$ and $\theta_i$ [10].

Second order moments of the scattering process can also be utilized to characterize the surface. The coherent complex Sinclair matrix, (or scattering matrix) can be expressed as [11] [12]:

$$\mathbf{S} = \begin{bmatrix} S_{HH} & S_{HV} \\ S_{VH} & S_{VV} \end{bmatrix} \quad (3)$$

Here $S$ is the measured complex scattering coefficients expressed in a horizontal and vertical basis. By vectorisation of $\mathbf{S}$ the Pauli target vector can be defined as

$$\mathbf{k} = \frac{1}{\sqrt{2}}[S_{HH} + S_{VV}, S_{HH} - S_{VV}, 2S_{HV}]^T \quad (4)$$

when considering the monostatic backscattering case, and assuming reciprocity. From $\mathbf{k}$, the polarimetric coherency matrix matrix is estimated as:

$$\mathbf{T_3} = \langle \mathbf{k}\mathbf{k}^{*T} \rangle \quad (5)$$

Here $\langle\rangle$ indicates averaging, usually in a local neighborhood, and $*T$ is the complex conjugate transpose. An eigendecomposition of the polarimetric coherency matrix $\mathbf{T_3}$ allows us to compute polarimetric features such as the Entropy $H$, Anistropy $A$, and Alpha angle $\alpha$. They all gives additional information about the scattering process. The entropy $H$ represents a measure of the randomness of the scattering mechanism. A high value of entropy indicates that there is not a dominating scattering mechanism, and low value indicates that we have a dominating scattering mechanism. The anistropy $A$ gives additional information about the scattering process in situations of high $H$. The alpha angle $\alpha$ indicates the type of scattering mechanism. It is independent of roughness and is found to increase with soil moisture so similar to the copolarizaton ratio it can be used to estimate $\epsilon^{'}$ [13].

Allain [14] proposes a surface parameter inversion algorithm under the Integral Equation Model (IEM) which has a larger validity range than SPM. The results show that for varying $kl$ the polarimetric feature ERD (Eigenvalue Relative Difference) was most suitable for inversion of $ks$. The ERD is computed from $\mathbf{T}_3$ when assuming reflection symmetry. Reflection symmetry is hypothesises that the correlation between co- and cross polarized channels is zero for natural media. From $T_3$ Non-ordered in size (nos) eigenvalues are derived as given in [11]. Allain's work also show that $\alpha_1$ (angle associated with the first eigenvector) is most suitable for inversion of $\epsilon^{'}$ for high frequencies.

# 4 Preliminary results and interpretation

The mean intensity is computed for VV, HH and HV for two of the measurements, that were taken after the oil was injected on the granular ice. The first measurement is from the day after oil injection (Day 14), when the oil was incapsulated in the ice but not visible at the surface. The second measurement considered, was from day 19, which was in the melting phase of the experiment, and the oil was visible at the surface. The region illuminated can be seen in the lower part of the images in **Figure 3**.

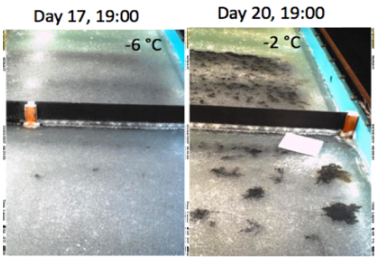


**Figure 3:** Timelapse camera showing the columnar ice at the upper part of the image, and the granular ice at the bottom, both interacting with a crude oil. The first and the last day of the ice melting phase is shown.

**Figure 4** shows mean intensity plots as function of incidence angle $\theta$.

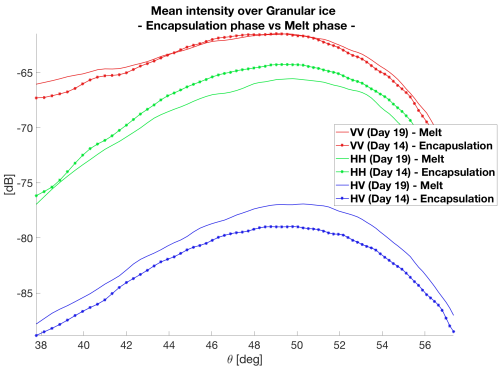

**Figure 4:** Mean intensity as a function of $\theta$. Day 14 (dotted line) representing the encapsulation phase of the experiment and day 19 (solid line) representing the melt phase of the oil-in-ice experiment. VV mean intensity is shown in red, HH mean intensity is shown in green while HV mean intensity is shown in blue.

Before computing the mean intensity, the data is multilooked by a $5 \times 5$ sliding window. The data has not been fully calibrated, and the antenna pattern is causing the shape of the curves we see in the intensity plot. However, we here assume that the dataset is well focused and that the two dates are comparable since the VV backscatter intensity is close to coinciding. We notice a decrease in HH, which indicates an change in copolarization ratio and thus may represent a change in the dielectric properties of the surface. The increasing VH channel may be related to surface roughness changes. The change of dielectric properties is consistent with the surface having an increased temperature from day 14 to day 19 but also the surface was a mix of oil and ice at this stage.

# 5 Conclusions and further work

A unique dataset from a ground based SAR data covering oil contaminated, laboratory grown saltwater ice is presented. Our preliminary investigations of the experimental data show a potential for using polarimetry analysis to characterise the surface. In order to investigate this in more detail, additional corrections and calibrations of the data is needed. Herein antenna pattern and gain corrections and estimating the antenna positions from the data.

# 6 Acknowledgements

The experiments were supported by the Research Council of Norway PETROMAKS2 program, grant number 243812 (MOSIDEO), and Center for Research Innovation (SFI) CIRFA, grant number 237906. We want to acknowledge all participants of the MOSIDEO/CIRFA experiment, especially Frédéric Boutet, Laurent Cronier and Lekhmissi Harkati who were part of the team collecting the GB-PoSAR data. We also want to thank STATOIL for providing crude oil to the experiment.

# References

[1] L. C. Smith and S. R. Stephenson, "New trans-arctic shipping routes navigable by midcentury," *Proceedings of the National Academy of Sciences*, vol. 110, no. 13, pp. E1191–E1195, 2013.

[2] M. Fingas and B. Hollebone, "Review of behaviour of oil in freezing environments," *Marine Pollution Bulletin*, vol. 47, no. 9–12, pp. 333 – 340, 2003.

[3] D. Dickins, "Behavior of oil spills in ice and implications for arctic spill response," in *OTC Arctic Technology Conference*, Offshore Technology Conference, February 2011.

[4] C. Brekke, B. Holt, C. Jones, and S. Skrunes, "Discrimination of oil spills from newly formed sea ice by synthetic aperture radar," *Remote Sensing of Environment*, vol. 145, pp. 1 – 14, 2014.

[5] W. F. Weeks, *On Sea Ice*. University of Alaska Press, 2010.

[6] B. Rekioua, M. Davy, L. Ferro-Famil, and S. Tebaldini, "Snowpack permittivity profile retrieval from tomographic sar data," *Comptes Rendus Physique*, vol. 18, no. 1, pp. 57 – 65, 2017. Prizes of the French Academy of Sciences 2015 / Prix de l'Académie des sciences 2015.

[7] T. G. Yitayew, L. Ferro-Famil, T. Eltoft, and S. Tebaldini, "Tomographic imaging of fjord ice using a very high resolution ground-based sar system," *IEEE Transactions on Geoscience and Remote Sensing*, vol. 55, pp. 698–714, Feb 2017.

[8] K.-H. D. Leung Tsang, Jin Au Kong, *Scattering of Electromagnetic Waves: Theories and Applications*. John Wiley & Sons, Inc., 2000.

[9] S. O. Rice, "Reflection of electromagnetic waves from slightly rough surfaces," *Communications on Pure and Applied Mathematics*, vol. 4, no. 2-3, pp. 351–378, 1951.

[10] M. R. K.-F. A. K. Ulaby, F. T., *Microwave remote sensing: Active and passive. Volume 2 - Radar remote sensing and surface scattering and emission theory*. Artec House, inc, 1982.

[11] J.-S. Lee and E. Pottier, *Polarimetric Radar Imaging from basics to application*. CRC Press, Taylor & Francis Group, 2009.

[12] S. R. Cloude and E. Pottier, "A review of target decomposition theorems in radar polarimetry," *IEEE Transactions on Geoscience and Remote Sensing*, vol. 34, pp. 498–518, Mar, 1996.

[13] I. Hajnsek, E. Pottier, and S. R. Cloude, "Inversion of surface parameters from polarimetric sar," *IEEE Transactions on Geoscience and Remote Sensing*, vol. 41, pp. 727–744, April 2003.

[14] S. Allain, *Caractérisation d'un sol nu à partir de données SAR polariméetriques. Etude multi-fréquentielle et multi-résolutions*. PhD thesis, Université Rennes 1, 2003.